A high Reynolds number algorithm for polytropic accretion disk studies

Michiel D. Nauta and Gábor Tóth[*]

Astronomical Institute, Utrecht University, P.O. Box 80 000, 3508 TA Utrecht, The Netherlands

Abstract. An algorithm is proposed to study two-dimensional vortices in thin, polytropic accretion disks. It is based on a method which has been used to study vortices in planetary atmospheres. It is special in that it conserves both energy and potential enstrophy in the absence of dissipation. This leads to desirable stability properties which permit calculations at relatively high Reynolds numbers. The algorithm is tested and compared to existing methods, in particular with a Total Variation Diminishing method.

Key words: accretion, accretion disks – hydrodynamics – turbulence – methods: numerical

1. Introduction

To explain the "anomalous" large viscosity in a *thin* accretion disk different routes have been tried. Very successful is the approach using magnetic fields (Balbus & Hawley, 1991; Hawley & Balbus, 1991; Geertsema & Achterberg, 1992; Schramkowski, 1996). A magnetic field can link fluid parcels at different radii. Because of the differential motion, the magnetic field is stressed and transfers angular momentum from the innermost to the outermost parcel. The result is that an initial (small) radial separation of the fluid parcels increases. If this process occurs among neighboring parcels then this mechanism drives the Velikhov-Chandrasekhar magneto-hydrodynamic (MHD) instability which amplifies the magnetic field and is responsible for MHD-turbulence (e.g. Brandenburg et al. 1995). Another source of MHD-turbulence could be due to the buoyancy of magnetic flux tubes. This MHD-turbulence might explain the enhanced transport in an accretion disk. If the fluid parcels are connected by coronal magnetic field so that they can be further apart, then it was shown (Aly & Kuijpers, 1990) that transport of angular momentum is particularly effective and requires a non-local description (Kuijpers, 1995).

The hydrodynamic route faces more trouble. Pure hydrodynamic convection has been suggested but was found to transport angular momentum inwards in stead of outwards e.g.

(Balbus et al., 1996). Shear-driven instabilities have been proposed but pure Keplerian rotation is linearly stable so that a non-linear instability is needed to drive the turbulence (Zahn, 1990). One example of such a non-linear instability which might occur in an accretion disk is given as the last test case in this paper. It is known as the instability of sheared disturbances (Haynes, 1987). However, even though this quasi-Keplerian rotation does get unstable, the instability does not extract energy from the Keplerian shear, but merely from the disturbance superposed on the Keplerian profile. This is in agreement with the finding of Balbus et al. (1996) that it is impossible to transfer energy from the Keplerian flow into both the radial and the azimuthal fluctuating velocity components. One of these always returns its energy to the mean flow.

If the flow deviates from Keplerian, hydrodynamic instabilities can be expected. This can occur at the inner edge of the disk where it is in contact with the compact object or at the outer edge where matter impinges on the disk. Also throughout the disk the Keplerian flow can be distorted by magnetic fields. These instabilities might give rise to two-dimensional vortices or eddies and these are the topic of some recent hydrodynamic work (Abramowicz et al., 1992; Kuijpers, 1995; Adams & Watkins, 1995). Large-scale 2-D vortices in disks had already been proposed by von Weizsäcker (1944). Also the work of Dubrulle was pointing in this direction (Dubrulle & Valdettaro, 1992). However, so far, numerical simulations of thin accretion disks have never given any hint for the existence of persistent vortices in disks [1].

Research of vortices and the related phenomenon of an inverse energy cascade in two dimensions relies heavily on direct numerical simulations. A breakthrough in this field was achieved when simulations could be done with a high Reynolds number (McWilliams, 1984). These simulations have put the ideas about inverse energy cascade and the associated emergence of coherent structures or vortices out of random initial conditions on a firm basis. Over the years this approach of using direct high-Reynolds number numerical simulations to study (quasi-) two-dimensional turbulence has developed from solving the 2-D incompressible Euler equations on a periodic Carte-

---

[1] We learned about very recent simulations showing long-lived vortices (Bracco et al., 1998) only after completion of this article

sian grid (McWilliams, 1984) into solving the shallow-water equations on the surface of a sphere (Cho & Polvani, 1996a). The latter simulation demonstrated the emergence of vortices and jets in decaying shallow-water turbulence on the surface of a fast spinning planet, and was specifically undertaken to model the flow on the four giant outer planets (Cho & Polvani, 1996b). Usually this kind of simulation is done with a pseudo-spectral code with very little dissipation. The small dissipation is often achieved by replacing the Laplacian with a higher order operator, e.g. biharmonic diffusion.

Because of the supersonic nature of the flow in thin accretion disks, simulations have been done with methods capable of representing shock waves e.g. (Różyczka & Spruit, 1993). Numerical oscillations generated at shock fronts are usually suppressed by introducing strong numerical diffusion. This can lead to unacceptably low Reynolds numbers that severely limit the ability to study turbulence. Here another choice is made. Initial conditions and parameters are chosen such that shocks don't occur and when they do and give trouble we terminate the calculation. This allows us to use techniques from geophysical fluid dynamics (GFD) that are more appropriate to the above mentioned high Reynolds numbers.

In this paper a simple numerical algorithm is proposed to solve the equations of a simplified model of an accretion disk. It can't handle shocks because of Gibbs oscillations but it does simulations at a high Reynolds number. The algorithm originates from GFD (Arakawa & Lamb, 1981) where it has been used very successfully to simulate parts of Jupiter (Williams & Wilson, 1988; Dowling & Ingersoll, 1989). If persistent vortices exist in accretion disks, this algorithm is a very likely candidate to find them. After discussing the equations and their approximations in Sect. 2 and the algorithm in Sect. 3, a number of numerical experiments demonstrate the performance of the algorithm (Sect. 4). Some of these test cases are used to compare the behavior of this algorithm with a shock capturing method as implemented in the freely available Versatile Advection Code (VAC) (Tóth & Odstrčil, 1996; Tóth, 1997). Actual simulations of vortices in an accretion disk will be presented in a following paper.

2. The equations

In this section it is shown that, under a number of assumptions, the equations describing the dynamics of a planetary atmosphere, which behaves as an incompressible fluid, are very similar to the compressible gas equations describing the dynamics in an accretion disk. The reason is that though the atmosphere is to a very good approximation incompressible ($\nabla \cdot \boldsymbol{v} = 0$), the two-dimensional divergence of the horizontal velocity need not be zero as the atmosphere can increase in thickness. In this way a hydrostatic thin layer of incompressible fluid mimics a compressible two-dimensional gas. Because of this similarity, identical discretisations can be used for both systems. First, the equations of a planetary atmosphere are discussed, then those of an accretion disk.

We stress that not *all* aspects of the dynamics of a three dimensional *incompressible* flow can be represented by a *compressible* 2D gas, e.g. vortices in the vertical direction have no corresponding counterpart. For planetary atmospheric applications, however, the analogy works quite well.

2.1. The shallow-water equations

In the study of planetary atmospheres a number of different models are being used to describe the dynamics, the simplest of which is the shallow-water model. It describes the evolution of an ideal, thin, homogeneous layer of fluid under the simultaneous influence of the effective gravity and the Coriolis force. The corresponding equations are derived from the incompressible Euler equations under the assumption that the fluid layer is thin, homogeneous, and in hydrostatic equilibrium in the third dimension (Pedlosky, 1987, Sect. 3.3). The most important step in the derivation is the integration of the hydrostatic equation in the vertical direction, which allows the horizontal pressure gradient to be expressed as the gradient of the free surface height h:

$$\frac{\partial \boldsymbol{v}}{\partial t} + q(\hat{z} \times h\boldsymbol{v}) + \nabla(\frac{1}{2}v^2 + \Phi) = 0, \tag{1}$$

$$\frac{\partial h}{\partial t} + \nabla \cdot (h\boldsymbol{v}) = 0,$$

$\boldsymbol{v}$ is the 2-D horizontal velocity, t is the time, q the potential vorticity $q = (f + \hat{z} \cdot \nabla \times \boldsymbol{v})/h$, f the planetary vorticity $f = 2\boldsymbol{\Omega} \cdot \hat{z}$, $\boldsymbol{\Omega}$ is the angular rotation frequency of the coordinate system (or the planet), $\hat{z}$ the unit vector in the local vertical direction, h the height of the free surface, and Φ the geopotential per unit mass $\Phi = gh$, with g the gravitational acceleration. These equations can be combined into one which describes the advection of potential vorticity:

$$\frac{\partial q}{\partial t} + \boldsymbol{v} \cdot \nabla q = 0. \tag{2}$$

Because the potential vorticity depends on the velocity, this equation describes advection of an active scalar, which is not easy to solve. A numerical scheme that solves the shallow-water equations should satisfy this advection property of potential vorticity in the best possible way.

Usually, discretisations of Eq. (1) require some form of viscosity to stabilize the small scales. However, the system exhibits an inverse cascade of kinetic energy in the rotational part of the velocity field and this could limit the unstable behavior on the small scales. The inverse cascade follows from the conservation of energy and potential enstrophy (assuming that the net flux of these quantities through the boundaries of the domain remain zero). Firstly, conservation of energy implies:

$$\frac{\partial}{\partial t} \int \int \left(\frac{1}{2}hv^2 + \frac{1}{2}gh^2\right) dA = 0,$$

and secondly, conservation of potential enstrophy:

$$\frac{\partial}{\partial t} \int \int \left(\frac{1}{2}hq^2\right) dA = 0.$$

Since the potential enstrophy is conserved, the ordinary enstrophy has a constant upper bound:

$$\int\int \left(\frac{1}{2}h^2q^2\right)dA \leq \int\int \left(\frac{1}{2}h_{\max}hq^2\right)dA.$$

From this point to arrive to the inverse energy cascade is very similar to the 2-D incompressible case (Pedlosky, 1987, Sect. 3.28). In Fourier space the relative enstrophy can be written as ($\boldsymbol{k}$ is the 2-D wave vector, the planetary vorticity is neglected here):

$$\int_0^\infty \int_0^\infty \frac{1}{2}|\boldsymbol{k}\times\boldsymbol{v}|^2 d^2\boldsymbol{k}$$
$$= \int_0^\infty \int_0^\infty \frac{1}{2}\left(k^2v^2 - (\boldsymbol{k}\cdot\boldsymbol{v})^2\right) d^2\boldsymbol{k}$$
$$= \int_0^\infty \int_0^\infty k^2 E_{\rm rot}(k)d^2\boldsymbol{k},$$

$E_{\rm rot}(k)$ is the kinetic energy density in 2D $\boldsymbol{k}$-space per unit mass of the rotational component of the velocity. If the rotational part of the kinetic energy is conserved (which is a reasonable approximation because of conservation of total energy) and nonlinear interactions move part of that energy to higher wave numbers, then the upper bound on the enstrophy implies that the bulk of that energy moves to lower wave numbers. It cascades in the inverse direction, all very analogous to the inverse cascade in 2D-incompressible fluids.

If it is possible to write a numerical algorithm for the shallow-water equations such that the discretised equations conserve energy and potential enstrophy, then part of the instability problems of ordinary codes at large wave numbers will not occur because of the correct energy cascade. For this reason it may be expected that, with such an energy and potential enstrophy conserving code, stable simulations are possible at higher Reynolds numbers than with a code that does not enforce the correct energy cascade. Arakawa & Lamb (1981) wrote an algorithm which satisfies both conservation properties. For completeness the algorithm is given in Sect. 3.

As already hinted at, this code still requires some dissipation (Bennett & Haidvogel, 1983). This is because the enstrophy is cascading in the ordinary direction, towards large wave numbers. If there was no dissipation, enstrophy would pile up at the largest wave number and would give rise to non-physical oscillations. This process is sometimes called enstrophy equipartitioning. In real space this would show up as sharp conspicuous peaks in the spatial distribution of potential vorticity. To suppress such peaks the dissipation process needs to be large enough.

Different forms of the dissipation operator are in use. This is, because for high Reynolds number flow, the grid resolution is insufficient to describe the phenomena taking place at the dissipation scale. Consequently, the dissipation operator should not describe molecular viscosity but the influence of sub-grid scale motions. Although a physically well funded representation of sub-grid scale motions is not known, it is common pratice to use a Laplacian operator to some power. That is why the right hand side of Eq. 1 is replaced with (for all three equations):

$$-\nu(-\nabla^2)^\alpha.$$

where the dot stands for the velocity component or the height respectively. A value for α of unity is appropriate for molecular viscosity (in an incompressible medium), while α larger than unity is called hyperviscosity. A special form of hyperviscosity is biharmonic diffusion: $\alpha = 2$. By increasing α the dissipation operator gets more selective. The same amount of dissipation (of potential enstrophy in 2D-simulations) can be achieved over a shorter range of wave numbers, allowing for a larger inertial range. So it is as if a higher Reynolds number flow is simulated if α is increased. A different way to achieve this effect is to use a larger grid which is not always possible because of limited computational resources. This explains the popularity of hyperviscosity in high Reynolds number research. The physical implications of its use are ill understood and the topic of many controversies. Some physical phenomena, such as the existence of an inverse energy cascade and the formation of coherent structures, are robust. Others, such as the slope of the spectrum in the inertial range, do depend on the form of viscosity (Cho & Polvani, 1996a). Since it has been used so widely it seems justified to apply it here (with care) as well.

2.2. The polytropic gas equations

The equations describing the dynamics in an accretion disk are not the shallow-water equations but the MHD equations with radiative transfer. However to explore possible similarities between flow in planetary atmospheres and in accretion disks, a number of simplifying assumptions can be made so that the resulting equations are similar to the shallow-water equations. Firstly, the effects of magnetic fields and radiative transfer are neglected. Secondly, the disk is assumed to be thin and in hydrostatic equilibrium so that the equations can be integrated over the height of the disk resulting in a two dimensional description. A further simplification is required because the resulting equations don't just advect potential vorticity but also produce it by the baroclinic term:

$$\frac{\nabla\Sigma \times \nabla P}{\Sigma^2},$$

where the pressure should be interpreted as the height integrated pressure and Σ stands for the height integrated density. To eliminate this production term and to focus on the dynamics, keeping the energetics as simple as possible, a polytropic equation of state is assumed:

$$P = K\Sigma^\gamma.$$

This assumption simplifies the baroclinic model to a barotropic one. For a planetary atmosphere it is known from observations that a barotropic model (the shallow-water equations) already describes many interesting phenomena. Unfortunately such observations are missing for an accretion disk, but assuming a polytropic relation is quite common in theoretical studies, e.g. (Goldreich et al., 1986). The resulting equations are:

$$\frac{\partial \boldsymbol{v}}{\partial t} + q(\hat{z}\times\Sigma\boldsymbol{v}) + \nabla\left(\frac{1}{2}v^2 + \Phi\right) = 0, \qquad (3)$$

$$\frac{\partial\Sigma}{\partial t} + \nabla\cdot(\Sigma\boldsymbol{v}) = 0,$$
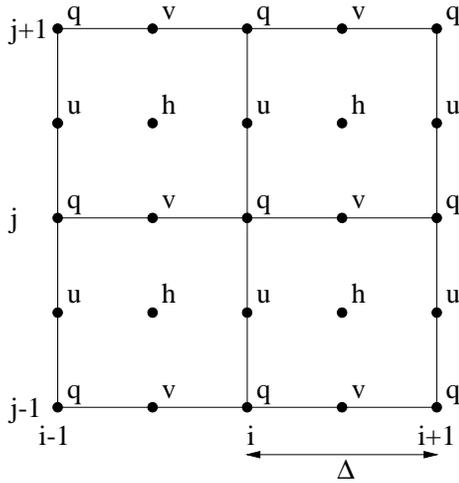
Fig. 1. The staggered Arakawa C grid.

Fig. 2. Flow geometry for shearing instability.

where q is the potential vorticity $q = (f + \hat{z} \cdot \nabla \times \boldsymbol{v})/\Sigma$ and $\Phi = \gamma P/((\gamma - 1)\Sigma) - GM/r - \Omega^2 r^2/2$ contains the enthalpy and the effective gravitational potential (due to the central compact object). The similarity with the shallow-water Eqs. (1) is obvious. The 2D polytropic gas equations, in the absence of a gravitating central object, even become identical to the shallow-water equations (replacing h with Σ) if $\gamma = 2$ (making Φ a linear function of Σ) and if $g = 2K$. It goes without saying that the waves of both sets of equations are basically the same, they just have different names, i.e. gravity waves in the shallow-water case versus sound waves in the polytropic case. Because of this similarity of the equations, an identical algorithm can be used both for the shallow-water equations and for the polytropic gas equations. As the conservative discretisation of Arakawa and Lamb has proven to be successful in the research of vortices on Jupiter (Williams & Wilson, 1988; Dowling & Ingersoll, 1989), it was decided to use this algorithm also to study vortices in accretion disks.

3. The algorithm

The Arakawa-Lamb scheme discretises the spatial part of the differential Eqs. (1) and (3) to second order. The time integration can be done with a standard method such as leap-frog or Runge-Kutta. The scheme uses a staggered grid known as the Arakawa C grid, see Fig. 1. The grid shows that the dependent variables are not calculated at every location. For example, to update the horizontal velocity component u at location $i, j + 1/2$, the velocity component v is needed at that same location $i, j + 1/2$ but according to Fig. 1 it is unknown here. By taking a linear combination of this velocity component in the surrounding grid points, i.e. at $i+1/2, j; i+1/2, j+1; i-1/2, j$ and $i-1/2, j+1$, some freedom is introduced in the discretisation. This degree of freedom is used to satisfy the constraints of conservation of both energy and potential enstrophy. These constraints determine which linear combinations have to be taken. The resulting algorithm (using the same notation as before) is given in Table 1. One of us (MDN) has implemented this algorithm together
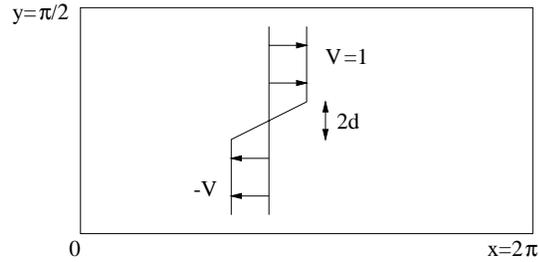
with the polytropic relation of Sect. 2.2 which is used to calculate Φ. Non-Cartesian grids are discretised by taking metric factors into account, so that the equations can also be used on the surface of a sphere or in a thin disk.

Boundary conditions are implemented with the help of ghost cells surrounding the computational domain. We use reflective and periodic boundary conditions in the test problems, since these allow us to check the conservation properties of the algorithms. Reflective boundaries are represented by updating the ghost cell values at every time step using the symmetry and anti-symmetry across the physical boundary, while periodic boundaries can also be implemented trivially. Other type of boundary conditions, like non-reflective, are perhaps possible with an appropriate extrapolation method.

4. Numerical experiments

In order to verify the performance of the code, it has been applied to a number of simple flow problems studied in the literature.

4.1. The shearing instability

In astrophysics this instability is better known as the Kelvin-Helmholtz instability. However in the geophysical context the latter term seems to be reserved for shearing instabilities in a stratified fluid. To avoid ambiguity the term shearing instability is used here.

Probably the most wide-spread astrophysical explanation of this instability makes use of Bernoulli's law. Geophysics offers a complementary description using Rossby waves (potential vorticity waves) which is also very illuminating, e.g. (Hoskins et al., 1985, Sect. 6). The flow pattern used in this calculation consists of a piecewise linear profile indicated in Fig. 2. The associated potential vorticity is negative and uniform in the shear layer. Suppose there is an infinitesimal sinusoidal displacement of the boundary of this strip as indicated in Fig. 3. The potential vorticity anomalies are marked with plus and minus signs. The velocities associated with these anomalies are indicated with dashed circles. The velocity field of the anomalies at the top of the potential vorticity strip propagate the top undulation to the left. The bottom wave moves to the right under the influence of its own velocity field. Both waves move in directions opposite to the local shear flow. These waves can be called Rossby waves and, depending on the phase velocity $v_{ph} = -\beta/(k_x^2 + k_y^2 + F^2)$, they might be (almost) stationary.

Table 1. The algorithm

$$\frac{\partial}{\partial t}h_{i+1/2,j+1/2} = -\frac{1}{\Delta}\left[u^*_{i+1,j+1/2} - u^*_{i,j+1/2} + v^*_{i+1/2,j+1} - v^*_{i+1/2,j}\right]$$

$$\frac{\partial}{\partial t}u_{i,j+1/2} = \alpha_{i,j+1/2}v^*_{i+1/2,j+1} + \beta_{i,j+1/2}v^*_{i-1/2,j+1} + \gamma_{i,j+1/2}v^*_{i-1/2,j} + \delta_{i,j+1/2}v^*_{i+1/2,j}-$$

$$\epsilon_{i+1/2,j+1/2}u^*_{i+1,j+1/2} + \epsilon_{i-1/2,j+1/2}u^*_{i-1,j+1/2} - \frac{1}{\Delta}\left[(K+\Phi)_{i+1/2,j+1/2} - (K+\Phi)_{i-1/2,j+1/2}\right]$$

$$\frac{\partial}{\partial t}v_{i+1/2,j} = -\gamma_{i+1,j+1/2}u^*_{i+1,j+1/2} - \delta_{i,j+1/2}u^*_{i,j+1/2} - \alpha_{i,j-1/2}u^*_{i,j-1/2} - \beta_{i+1,j-1/2}u^*_{i+1,j-1/2}-$$

$$\phi_{i+1/2,j+1/2}v^*_{i+1/2,j+1} + \phi_{i+1/2,j-1/2}v^*_{i+1/2,j-1} - \frac{1}{\Delta}\left[(K+\Phi)_{i+1/2,j+1/2} - (K+\Phi)_{i+1/2,j-1/2}\right]$$

with

$$u^*_{i,j+1/2} = \frac{1}{2}\left(h_{i+1/2,j+1/2} + h_{i-1/2,j+1/2}\right)u_{i,j+1/2}$$

$$v^*_{i+1/2,j} = \frac{1}{2}\left(h_{i+1/2,j+1/2} + h_{i+1/2,j-1/2}\right)v_{i+1/2,j}$$

$$\alpha_{i,j+1/2} = \frac{1}{24}\left[2q_{i+1,j+1} + q_{i,j+1} + 2q_{i,j} + q_{i+1,j}\right]$$

$$\beta_{i,j+1/2} = \frac{1}{24}\left[q_{i,j+1} + 2q_{i-1,j+1} + q_{i-1,j} + 2q_{i,j}\right]$$

$$\gamma_{i,j+1/2} = \frac{1}{24}\left[2q_{i,j+1} + q_{i-1,j+1} + 2q_{i-1,j} + q_{i,j}\right]$$

$$\delta_{i,j+1/2} = \frac{1}{24}\left[q_{i+1,j+1} + 2q_{i,j+1} + q_{i.j} + 2q_{i+1,j}\right]$$

$$\epsilon_{i+1/2,j+1/2} = \frac{1}{24}\left[q_{i+1,j+1} + q_{i,j+1} - q_{i,j} - q_{i+1,j}\right]$$

$$\phi_{i+1/2,j+1/2} = \frac{1}{24}\left[-q_{i+1,j+1} + q_{i,j+1} + q_{i,j} - q_{i+1,j}\right]$$

$$q_{i,j} = \frac{f + \frac{1}{\Delta}\left[v_{i+1/2,j} - v_{i-1/2,j} - u_{i,j+1/2} + u_{i,j-1/2}\right]}{\frac{1}{4}\left(h_{i+1/2,j+1/2} + h_{i+1/2,j-1/2} + h_{i-1/2,j+1/2} + h_{i-1/2,j-1/2}\right)}$$

$$K_{i+1/2,j+1/2} = \frac{1}{4}\left[u^2_{i+1,j+1/2} + u^2_{i,j+1/2} + v^2_{i+1/2,j+1} + v^2_{i+1/2,j}\right]$$
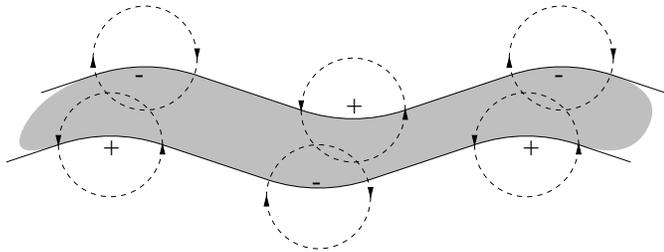

Fig. 3. Part of the negative potential vorticity strip associated with the flow geometry of Fig. 2. A wavy perturbation has been applied to investigate the stability. The plus and minus signs indicate the position where an excess or deficit of potential vorticity exists compared with the unperturbed potential vorticity strip. The rotation directions associated with the anomalies are indicated with dashed circles. The instability can be explained by the influence of the velocity field (at the location of the arrowheads) on the perturbed potential vorticity strip as discussed in the text.

Here β is the gradient in potential vorticity, k_x and k_y are the components of the wave vector, and F is the ratio of planetary vorticity to the speed of sound. Considering the influence of one Rossby wave on the other exposes the instability mechanism. Firstly, the almost stationary Rossby wave becomes truly stationary because it is opposed or helped (depending on the phase difference) in its propagation against the shear flow by the Rossby wave on the other side of the potential vorticity strip. Secondly, the undulation of one Rossby wave is positively correlated with the velocity of the other Rossby wave. This leads to growth of the wave amplitude.

This mechanical description of the shearing instability leads to a very clear understanding of a sequence of stability criteria which started with Rayleigh's inflection point criterion (Rayleigh, 1880) and culminated in the work of Arnol'd (1969). (For a very readable review consult Dowling (1995, Sect. Stability)). Firstly, a 2D-flow is stable if the velocity and the potential vorticity gradient are of opposite sign everywhere. Secondly, a flow is stable if the velocity and the potential vorticity gradient are of the same sign and the flow speed is larger than the phase speed of the fastest Rossby wave. Both criteria describe conditions that prevent the occurrence of stationary Rossby waves that can lock in phase.
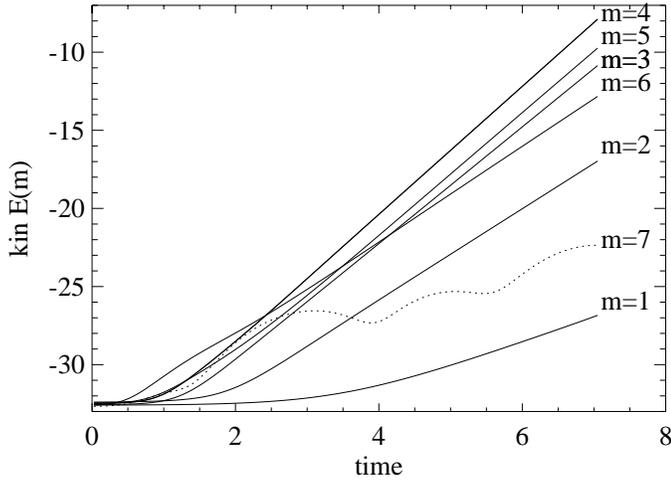
Fig. 4. Kinetic energy versus time for the shearing instability on a 64×64 grid. The first stable mode $m = 7$ is indicated with a dotted line.

This well studied instability is used here as a test to compare the analytical growth rate to the numerically simulated one. For this comparison, a very simple flow pattern is used, but the shearing instability also finds applications in more complicated situations such as the instability in thick accretion tori (Goldreich et al., 1986), where the principal branch can be associated with it. Here the simulation domain is rectangular, $2\pi \times \pi/2$, with two periodic and two reflective free-slip boundaries. (All quantities are in non-dimensional units.) Because of the periodic boundary conditions, only waves with a wavelength that is an integer fraction of 2π are admitted. So the wave modes have wave numbers: $k_x = 2\pi/\lambda = m$ with $m = 1, 2, 3....$ The equations solved are Eq. (1) with an initial piecewise linear velocity profile as indicated in Fig. 2. The shear layer has a width of $2d = 0.19$, the density is initially uniform ($\rho = 1$) and the Mach number $V/c_s = 0.1$ so that a sound wave crosses the width of the box approximately 6 times in one unit of time. Calculations are performed with a Courant number of 0.9. A small random perturbation of amplitude 10^{-10} is added to the velocity to start up the instability.

To calculate the growth rate of the instability, the kinetic energy per unit mass per wave number (k_x, k_y) has been calculated and is then summed over k_y. The logarithm of this energy $E(k_x)$ is plotted as a function of time for the 7 lowest wave modes in Fig. 4. The $m = 4$ and $m = 5$ modes are the fastest growing, which is in agreement with the rule of thumb that the most unstable wave has a wavelength of 2π times the width of the shear layer. The growth rates determined in this way are compared to analytical results (Ong & Roderick, 1972), Table 2. The growth rate has been scaled with the width of the shear layer (as in Ong & Roderick 1972), $\Gamma = \gamma d/V$ where γ is the measured growth rate. It is clear that the simulations are in agreement with linear stability theory. It can be concluded that the implementation is correct and that the code describes this kind of instabilities correctly.
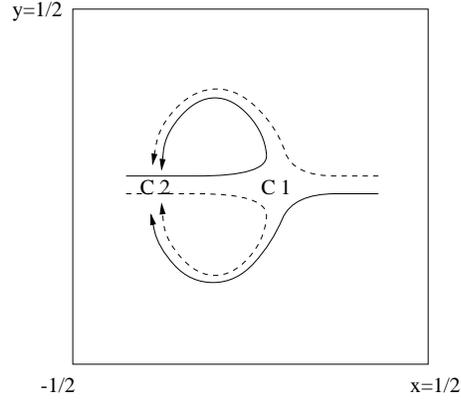

Fig. 5. Schematic path of the vortices. At C1 the first dipole collision occurs, at C2 another one might follow depending on the strength of the vortices. The two vortices with positive vorticity are indicated with solid lines, the two with negative vorticity with dashed lines.

Table 2. Comparison of the numerically calculated dimensionless growth rates of the shearing instability for three different resolutions and their analytical values from Ong & Roderick (1972).

mode	growth rate Γ		
m	analytical	32×32	64×64	128×128
1	0.082	0.074	0.077	0.078
2	0.143	0.131	0.138	0.139
3	0.182	0.165	0.177	0.179
4	0.199	0.178	0.194	0.197
5	0.190	0.174	0.187	0.187
6	0.140	0.155	0.145	0.140

4.2. The partner-exchange dipole vortex collision

This experiment was performed to compare the Arakawa-Lamb scheme with a typical shock-capturing algorithm. As a prototype of these methods, the Total Variation Diminishing (TVD) method of Harten (1983) as it is implemented in VAC (Tóth & Odstrčil, 1996; Tóth, 1997) has been used. TVD methods discretise a conservative hyperbolic system of equations, such as the shallow-water equations, with a limiting function applied to the fluxes to prevent numerical oscillations.

The experimental set up of this test is based on laboratory experiments of dipole collisions (Heijst & Flór, 1989) and the phenomena are schematically indicated in Fig. 5. In the experiment, dyed fluid was injected trough two small pipes on both sides of a square tank filled with a stratified fluid. First two turbulent plumes formed, then owing to the stratification the vertical velocity component collapsed, the fluid behaved as if it was two-dimensional, and two dipolar vortices formed. These traveled towards each other and collided. During the collision, opposite halves of each dipole bounded together to form two new dipoles. These new dipoles moved away from each other in the horizontal plane under an angle with respect to the original paths of the dipoles. Depending on the parameter setting, a second collision could follow.
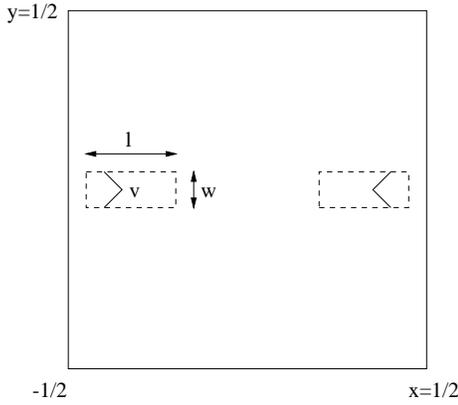
Fig. 6. Numerical initial condition for partner-exchange dipole collision. The dashed boxes give the area of the jet like structures. Their velocity profiles are indicated within these regions.

In an attempt to reproduce the above described process, Eq. (1) is solved numerically on a square domain. Initially two jet like structures are superimposed on a uniform state ($\rho = 1, v = 0, c_s = 4$) as shown in Fig. 6. In this figure the area of the "jet" is indicated with a dashed line. On this area the "jet" has a linear velocity profile: $v_x(y) = v_{max}(1 - 2|y|/w)$. In this way the injection of fluid through a pipe is simulated. The parameters for the left "jet" are: $l = 0.2, w = 0.1, v_{max} = 2$, and for the right "jet": $l = 0.2, w = 0.1, v_{max} = -1.5$. Because the "jets" are not of equal strength, this simulation is qualitatively very similar to the interaction described in (Heijst & Flór, 1989) which led to a second dipole collision.

This initial state is evolved in time both with the Arakawa-Lamb algorithm and with the TVD scheme with Woodward limiters with a Courant number of 0.9. The potential vorticity distribution at some typical times is displayed in Fig. 7. The last picture is taken at the moment that the vortices in the Arakawa-Lamb calculation are undergoing their second dipole collision C2. The vortices in the TVD calculation however, are just halfway between collision C1 and C2. This indicates that the TVD algorithm is much more diffusive in potential vorticity. The dipoles are larger and smoother, the peak potential vorticity is smaller and the propagation speed of the dipoles is lower. Also the distribution of potential vorticity is very smooth, which seems to be in disagreement with the dye distribution of the laboratory experiment (Heijst & Flór, 1989) and the Arakawa-Lamb calculation.

This diffusiveness is confirmed by the graph of the energy and potential enstrophy as a function of time, Fig. 8. For an ideal fluid these quantities should be conserved. However to prevent enstrophy pile-up (Sect. 2.1) a small ($\nu = 5 \cdot 10^{-10}$) biharmonic diffusion has been added to the Arakawa-Lamb scheme which explains the decrease in both energy and potential enstrophy. The influence of this small diffusion on the position of the vortices, as shown in Fig. 7, was found to be negligible because a calculation *without* diffusion ended with the vortices at the same location as in Fig. 7, however some suspicious spikes showed up which were attributed to enstrophy equipartitioning.
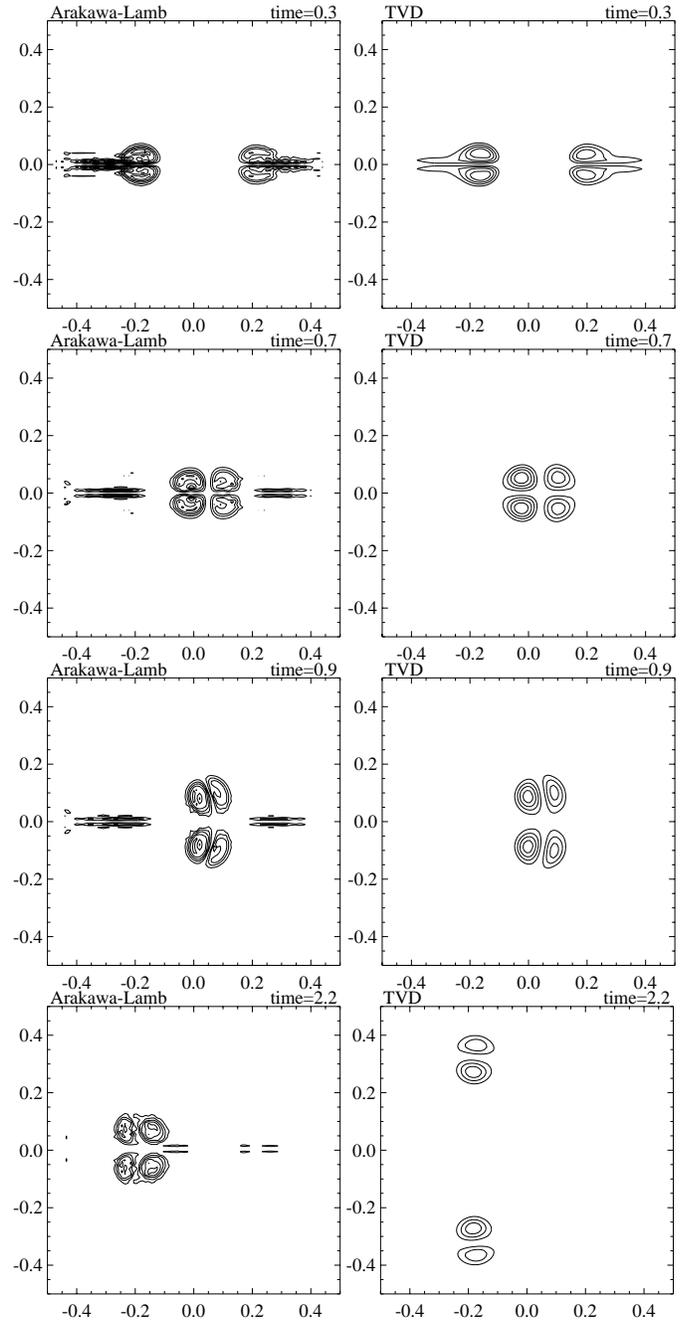

Fig. 7. Dipole vortex collision shown in potential vorticity for four different times. The left pictures show the simulation with our Arakawa-Lamb scheme, the right with TVD. The contour interval is 10 and the zero-contour has been left out.

Again the TVD calculation exhibits a much larger dissipation of energy and potential enstrophy, as seen in Fig. 8, confirming the diffusiveness of this algorithm. Also note that the decrease in potential enstrophy is only twice the decrease of energy in the TVD run, while for Arakawa-Lamb this ratio is almost 4. In 2D-turbulence simulations it is usually tried to make this ratio as large as possible.

A TVD run with a higher resolution should give results closer to the results of the Arakawa-Lamb scheme. With a
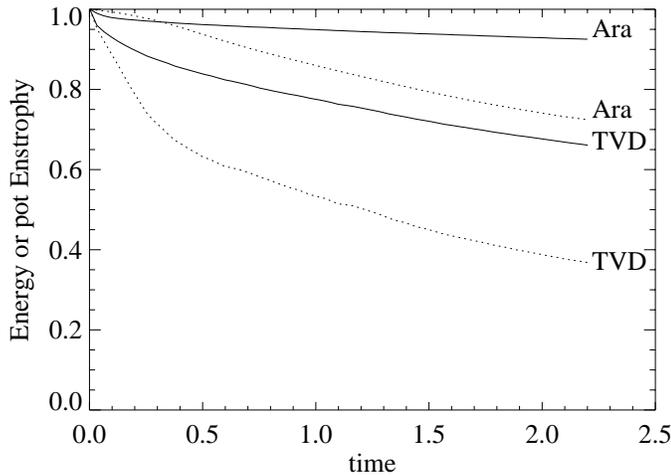
Fig. 8. Evolution of total energy (solid lines) and potential enstrophy (dotted lines) for the dipole collision for both numerical algorithms. All data are normalized to their initial values.
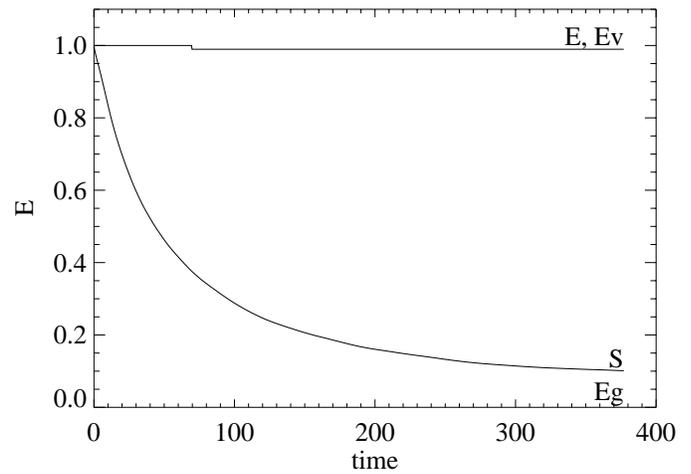

Fig. 9. Evolution of total energy (E), potential enstrophy (S), vortical energy (Ev) and energy in the compressible modes (Eg) for decaying shallow-water turbulence. Notice that the latter energy is almost zero during the whole run so that the total energy is practically equal to the vortical energy. The data was normalized with the initial energy and potential enstrophy respectively.
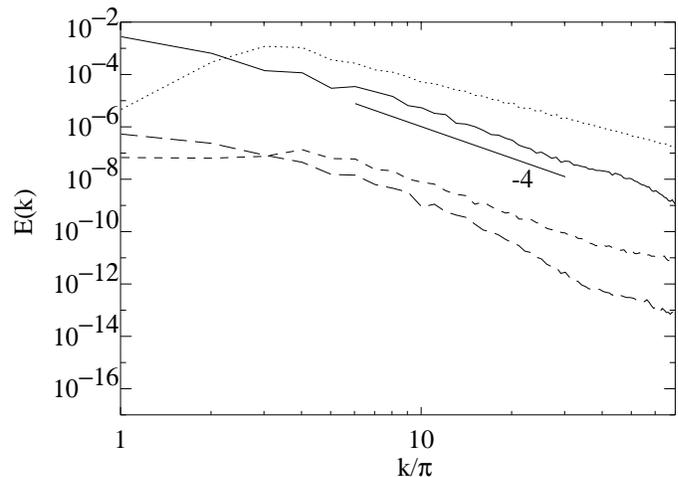

Fig. 10. Spectra of vortical energy (dotted line at $t = 0$, solid line at $t = 377$) and compressible energy (short dashed line at $t = 0$, long dashed line at $t = 377$) on a log-log plot. A straight line with slope -4 is shown for reference.

grid of 200×200 TVD gives similar positions for the dipoles at time=2.2 as shown in Fig. 7 for the Arakawa-Lamb calculation on a grid of 100×100. This shows that the Arakawa-Lamb scheme is much more efficient for these kind of problems.

4.3. Decaying shallow-water turbulence

In order to investigate how the Arakawa-Lamb scheme compares with a pseudo-spectral code, which is the prevailing method for 2D-turbulence simulations, the decaying shallow-water turbulence experiment of Farge & Sadourny (1989, FS) (their case BM) is repeated. In their article they distinguished two classes of eigenmodes: the divergent free vortical mode and two compressible modes with zero linearized potential vorticity. Their main findings were the existence of an inverse energy cascade in the vortical component of the flow, no energy exchange between the two classes of modes and the emergence of coherent vortices. In this paper all parameters and initial conditions are chosen as close as possible to the one described by FS, i.e. an initial Gaussian random field is evolved according to Eq. (1) up to time 377 on a square periodic domain on a grid of 256×256. The only exception is in the diffusion operator. FS used a ∇^{16} operator which is considered to be too high for a finite difference code, so here a ∇^8 operator is used instead.

The evolution of energy split into the two classes of eigenmodes (Ev: energy in vortical mode, Eg: energy in compressible modes), total energy and potential enstrophy is shown in Fig. 9 and is similar to Fig. 2a of FS. The potential enstrophy decreases rapidly by an order of magnitude, while the energy goes down with only 2 percent. This is typical for 2D-turbulence and in FS the decrease in energy was even less than 1 percent. In agreement with FS is the finding that the initial balanced state, which is a state in which $\nabla \cdot v = \partial\nabla \cdot v/\partial t = 0$, remains in balance equilibrium which is apparent because all the energy resides in the vortical component.

This is also clearly depicted in the energy spectra, Fig. 10, which is to be compared with Fig. 3a of FS. A power law spectrum with an index of -4 is seen in the vortical energy, which is commonly observed for 2D-turbulence. The energy spectrum of the compressible modes seems to have approximately the same slope, clearly different from FS where this spectrum is rather flat. This can partly be explained by the lower order of our diffusion operator. This moves the wavenumber at which the dissipation regime starts to lower values. Another part seems to be intrinsic to the algorithm.

Finally the spatial distribution of vorticity, potential vorticity, divergence of the velocity, stream function and height of free surface is shown in Fig. 11. A similar gray scale was used as in FS, their Fig. 6a. The vorticity and potential vorticity plots
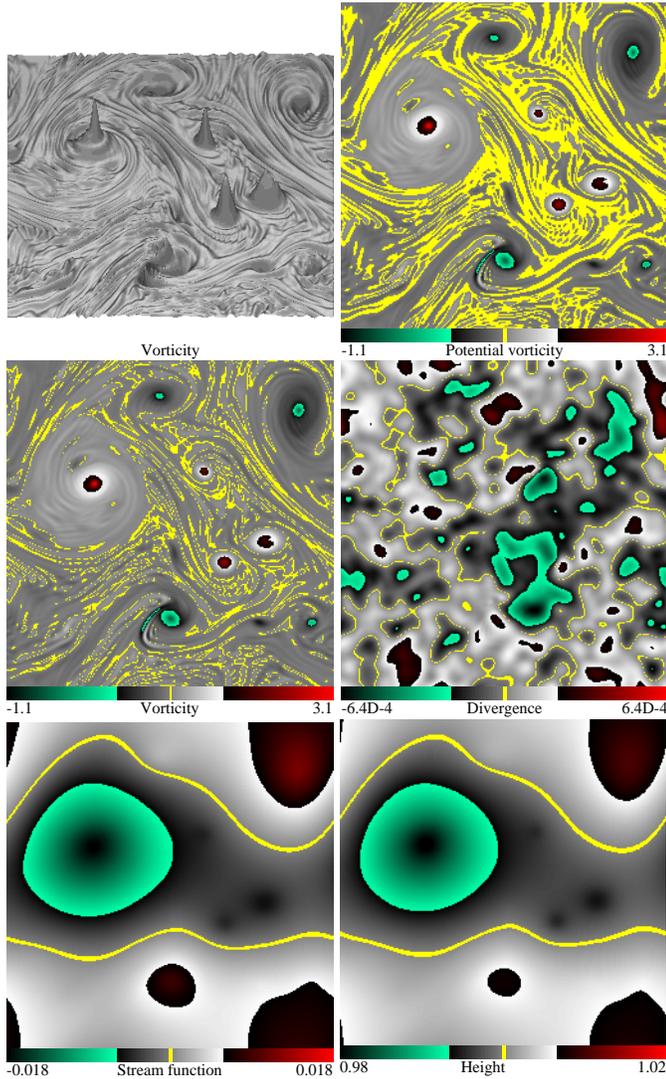
Fig. 11. Spatial distribution of vorticity in shade perspective representation and potential vorticity, vorticity, divergence of velocity, stream function and free surface height in cartographic representation at time=377 of an initially Gaussian random field.

show the coherent vortices very clearly. The divergence is still randomly distributed, but comparison with FS indicates that the high wave number compressible components are more damped in this finite difference calculation than in the pseudo-spectral one. This same conclusion was already drawn from the spectra. The stream function and the height are again in agreement with FS.

For comparison reasons, a similar calculation was done with the TVD method of VAC with the same settings as in Sect. 4.2 The shade perspective representation of the vorticity is given in Fig. 12. The flow field is clearly very much affected by the relatively large intrinsic viscosity of this algorithm.

The overall conclusion is that the simulation of the vortical component with this finite difference scheme is quite good, the same qualitative conclusions can be drawn from this simulation as Farge & Sadourny did from theirs. However some prudence
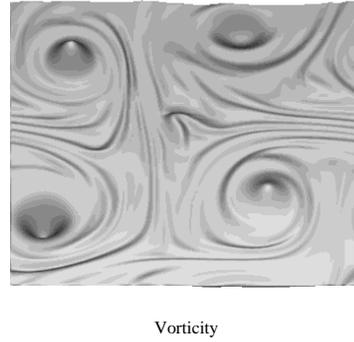

Fig. 12. Shade perspective representation as in Fig. 11 of the vorticity for a TVD calculation.
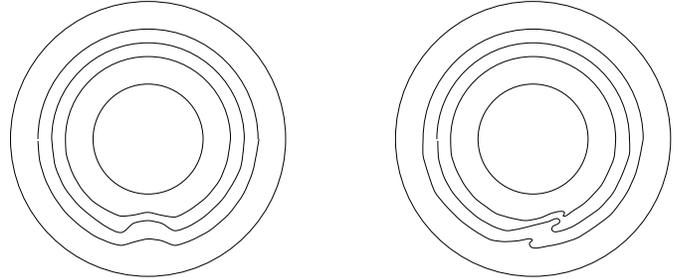

Fig. 13. Sketch of the potential vorticity contours in a Keplerian rotating disk with a initial disturbance (left) and the same disturbance after a while (right). Because the potential vorticity is mainly advected with the Keplerian flow inflection points of potential vorticity form naturally.

is called for if it comes to the high wave number compressible modes. They might be more damped than is desirable. This disadvantage should be contrasted with the advantage of a finite difference formulation which is more flexible in the sense that other non-Cartesian (but orthogonal) grids can easily be used with non-periodic boundary conditions.

4.4. A non-linear instability in a quasi Keplerian flow

This last test problem is astrophysically motivated and is related to stability issues in accretion disks (see also the introduction). Hydrodynamic stability of Keplerian flow has been a controversial point for a long time. However, at least one special type of instability seems very likely to develop in an accretion disk, the instability of sheared disturbances (Haynes, 1987). The mechanism of this instability is outlined here, for details consult the original publication.

Suppose there is a finite amplitude perturbation in the disk. For most disturbances the lines of constant potential vorticity will be distorted, for example as sketched in Fig. 13 on the left. The temporal development of this disturbance is governed by the advection equation for potential vorticity, Eq. (2). If the amplitude of the disturbance is not too large then the Keplerian flow dominates the advection. This deforms the disturbance as indicated in Fig. 13 on the right. Naturally the lines of constant potential vorticity bend over and develop a Z-shape. Rossby waves running along the diagonal of this Z-shape move to the
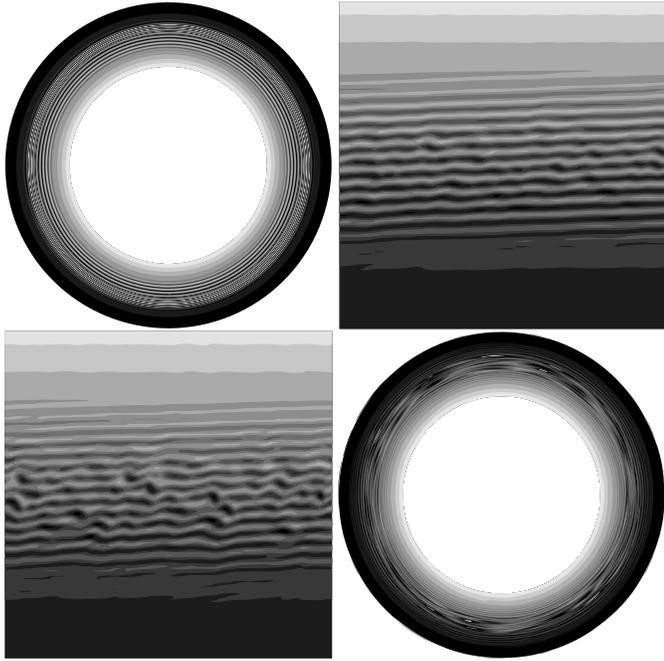
Fig. 14. The potential vorticity of the initial condition and after 9.6, 11.2 and 15.9 orbital periods for the sheared disturbance instability in a quasi Keplerian rotating disk. To show the instability more clearly, the data at 9.6 and 11.2 orbital periods is plotted as a square with angle along the horizontal and radius along the vertical axis.

left because the potential vorticity gradient is positive while on the horizontal branches they move to the right because of the negative potential vorticity gradient. As discussed in Sect. 4.1 for the shearing instability, this is a potentially unstable situation if the Rossby waves are fast enough to travel up against the shear (second stability criterion of Arnol'd). Since the phase speed of Rossby waves is proportional to the gradient in the potential vorticity and this quantity increases in time, in the end such fast Rossby waves will be possible. This instability can be prevented by viscosity, by limiting the maximum potential vorticity gradient achievable. Viscous effects for these kind of flow phenomena were discussed by Dubrulle & Zahn (1991).

To test the cylindrical grid and gravity, an initial condition was set up such that it was expected to show the behavior as described above. Similarly to Haynes, we save computer time by choosing an initial disturbance with an inflection point as depicted on the right panel of Fig. 13. Since the Keplerian shear $1.5\sqrt{GM/R^3}$ is much larger than typical potential vorticity gradients $0.75\sqrt{GM/R^5}$ and Arnol'd's second stability criterion should be violated, the initial disturbance is chosen to be much more sheared over then Haynes did. The disturbance takes the form of a tightly wound spiral as shown in Fig. 14 on the top left. The sheared disturbance is derived from the stream function:

$$\Psi = a_0 \frac{\cos(\kappa\phi + \lambda(R-r))}{\kappa^2 + \lambda^2} \exp\left(-(R-r)^6\right),$$

where R is the average radial distance of the disturbance and we have chosen $\kappa = 1$ and $\lambda = 6.4\pi$. The extra exponential

factor compared with Haynes was added because here reflective boundary conditions are used at the inner and outer edge of the disk at $0.75R$ and $1.25R$ respectively. The evolution in time is governed by Eq. (3) (where $\gamma = 1.4$ is used). Calculations are performed in a coordinate frame that rotates with the Keplerian speed at $r = R$. To obtain the non-dimensional parameters that determine the problem it is better to transform these equations to a shearing coordinate frame where Ω is a function of r and the complete Keplerian velocity is removed. The resulting non-dimensional parameters are: the *Rossby number* $Ro = U/2\Omega L$ (and $1/2\Omega T$) where U, L and T are the typical velocity, length and time scale of the non-Keplerian component of motion respectively; the *Mach number* $Ma = U/c_s$; and the *ratio of the sound speed and the Keplerian velocity* $c_s/v_k = c_s/\sqrt{(GM/R)}$. Typical parameters used are: $c_s/v_k = 0.1$, $Ma = 0.006$ (based on the disturbance), and $Ro = 0.002$. The grid is 128×128 and the diffusion time for one grid cell is typically 80 orbital periods. A small random perturbation starts up the instability, which can be seen in Fig. 14. We plot the potential vorticity after 9.6, 11.2 and 15.9 orbits around the compact object. The potential vorticity is broken up into patches of comparable width to the original spiral. This instability is not expected to drive turbulence because it seems that it does not extract energy from the Keplerian flow, only from the sheared disturbance. In this sense the results are in agreement with Balbus et al. (1996).

Shocks were not observed in these simulations although at the boundaries compressible phenomena developed that hardly showed up in the potential vorticity plots. Possible influence of the over-reflective instability (Narayan et al., 1987) was checked by repeating the simulation with a kind of absorbing boundary condition (Martinsen & Engedahl, 1987). The potential vorticity evolution was found to be very similar to the experiment with reflective boundaries indicating that over-reflection is not very important in this experiment on these timescales.

5. Conclusion

The main goal of this work is to present a numerical algorithm which is suited to investigate vortices in thin polytropic accretion disks, in particular to answer the question why large 2D-vortices have not been found in studies of disks so far, e.g. (Różyczka & Spruit, 1993), (Godon, 1997) and Brandenburg et al. (1995) even mention this explicitly. The algorithm is basically a shallow-water scheme from geophysical fluid dynamics (Arakawa & Lamb, 1981). Because of the similarity of the shallow-water equations with the 2D-polytropic gas equations, it can also be used to investigate thin polytropic accretion disks.

The tests performed demonstrate that the algorithm is well suited to describe instabilities of the shearing type also when they occur in an accretion disk in the form of instability of sheared disturbances (Haynes, 1987). In the latter case the instability does not seem to draw its energy from the Keplerian rotation but from the initial disturbance creating an inflection point. This is in agreement with the results from Balbus et al. (1996). Why these authors did not observe this phenomena can

only be guessed. They may not have waited long enough for the second stability criterion of Arnol'd to be violated or their Reynolds number may have been too low.

The essential aspects of 2D-turbulence are also simulated correctly with this algorithm. The inverse energy cascade is well represented and long lived coherent structures are seen to form out of random initial conditions as they should. This algorithm combines the low diffusivity needed for this kind of work with the flexibility of a finite difference formulation. Therefore, it is expected to be well suited to study vortices in accretion disks around compact objects and their influence on transport. Another interesting application is to study the role of vortices in planet formation in protoplanetary disks (Tanga et al., 1996). The main disadvantage of this algorithm is that it results in oscillations around discontinuities such as shocks. If these occur, shock-capturing methods such as TVD are preferable.

References

Abramowicz M. A., Lanza A., Spiegel E. A., Szuszkiewicz E., 1992, Nat 356, 41

Adams F. C., Watkins R., 1995, ApJ 451, 314

Aly J. J., Kuijpers J., 1990, A&A 227, 473

Arakawa A., Lamb V. R., 1981, Mon. Wea. Rev. 109, 18

Arnol'd V. I., 1969, Am. Math. Soc. Transl. Ser. 2 79, 267

Balbus S. A., Hawley J. F., 1991, ApJ 376, 214

Balbus S. A., Hawley J. F., Stone J. M., 1996, ApJ 467, 76

Bennett A. F., Haidvogel D. B., 1983, J. Atmos. Sci. 40, 738

Bracco A., Provenzale A., Spiegel E., Yecko P., 1998, Spotted Disks. In: Abramowicz A. (ed.), Proceedings of the Conference on Quasars and Accretion Disks. Cambridge Univ. Press

Brandenburg A., Nordlund Å., Stein R. F., Torkelsson U., 1995, ApJ 446, 741

Cho J. Y.-K., Polvani L. M., 1996a, Phys. Fluids 8, 1531

Cho J. Y.-K., Polvani L. M., 1996b, Sci 273, 335

Dowling T. E., 1995, Annu. Rev. Fluid Mech. 27, 293

Dowling T. E., Ingersoll A. P., 1989, J. Atmos. Sci. 46, 3256

Dubrulle B., Valdettaro L., 1992, A&A 263, 387

Dubrulle B., Zahn J.-P., 1991, J. Fluid Mech. 231, 561

Farge M., Sadourny R., 1989, J. Fluid Mech. 206, 433 (FS)

Geertsema G. T., Achterberg A., 1992, A&A 255, 427

Godon P., 1997, ApJ 480, 329

Goldreich P., Goodman J., Narayan R., 1986, MNRAS 221, 339

Harten A., 1983, J. Comp. Phys. 49, 357

Hawley J. F., Balbus S. A., 1991, ApJ 376, 223

Haynes P. H., 1987, J. Fluid Mech. 175, 463

Heijst G. J. F. v., Flór J. B., 1989, Nat 340, 212

Hoskins B., McIntyre M., Robertson A., 1985, Q. J. R. Meteorol. Soc. 111, 877

Kuijpers J., 1995, Flares in Accretion Disks. In: Benz A. O., Krüger A. (eds.), Proc. CESRA Workshop Caputh, Coronal Magnetic Energy Releases, Vol. 444 of Lecture Notes in Physics. Springer Verlag, Berlin, p. 135

Martinsen E., Engedahl H., 1987, Coastal Eng. 11, 603

McWilliams J. C., 1984, J. Fluid Mech. 146, 21

Narayan R., Goldreich P., Goodman J., 1987, MNRAS 228, 1

Ong R. S., Roderick N., 1972, Planet. Space Sci. 20, 1

Pedlosky J., 1987, Geophysical Fluid Dynamics. Springer-Verlag, Berlin

Rayleigh L., 1880, Proc. London Math. Soc. 111, 57

Różyczka M., Spruit H., 1993, ApJ 417, 677

Schramkowski G. P., 1996, A&A 308, 1013

Tanga P., Babiano A., Dubrulle B., Provenzale A., 1996, Icarus 121, 158

Tóth G., 1997, Versatile Advection Code. In: Hertzberger B., Sloot P. (eds.), High-Performance Computing and Networking, Vol. 1225 of Lecture Notes in Computer Science. Springer Verlag, Berlin, p. 253

Tóth G., Odstrčil D., 1996, J. Comp. Phys. 128, 82

von Weizsäcker L. F., 1944, Zeitschrift für Astrophysik 22, 319

Williams G. P., Wilson R. J., 1988, J. Atmos. Sci. 45, 207

Zahn J.-P., 1990, On the Nature of Disk Viscosity. In: Bertout C., Collin-Souffrin S., Lasota J., Tran Thanh Van J. (eds.), Structure and Emission Properties of Accretion Disks. Editions Frontières, Gif sur Yvette, p. 87